



Article

Failure Mode of Deep-Buried Rectangular Chamber and Upper Bound Solution of Surrounding Rock Pressure

Daobing Zhang ^{1,2}, Linhai Zeng ^{1,2,*}, Zhilin Lv ³, Xiaochuan Yu ³, Chang Liu ³, Anming Jiang ², Xianyong Jiang ², Qi Li ² and Yongxiang Yang ²

- Sanya Institute of Hunan University of Science and Technology, Sanya 572024, China; dbzhang@hnust.edu.cn
- School of Resource Environment and Safety Engineering, Hunan University of Science and Technology, Xiangtan 411201, China; jianganmin123@126.com (A.J.); 24300101003@mail.hnust.edu.cn (X.J.); 23020103021@mail.hnust.edu.cn (Q.L.); 22020101049@mail.hnust.edu.cn (Y.Y.)
- ³ China Gezhouba Group Road & Bridge Co., Ltd., Yichang 443002, China; zllv0073@cggc.cn (Z.L.); yuxc81@163.com (X.Y.); cliu0045@cggc.cn (C.L.)
- * Correspondence: 22300101005@mail.hnust.edu.cn; Tel.: +86-13902203157

Abstract: In order to obtain more reasonable failure modes and more precise surrounding rock pressures of deep-buried underground rectangular chambers, the failure mode of a "wedge-shaped collapse body + arc rotator + logarithmic spiral rotator" deep-buried chamber is constructed based on the analysis of existing failure mode. The upper bound solution of the surrounding rock pressure is derived based on limit analysis. The validity of the proposed failure model and the reliability of the limit analysis approach are demonstrated through numerical simulations, theoretical verification, and comparisons with engineering practices. The influence of various parameters on surrounding rock pressure is analyzed. The results show that each parameter has different influence on the surrounding rock pressure. The surrounding rock pressure q and e increases linearly with the increase in rock gravity γ and chamber size, and decreases with the increase in cohesion e0 and internal friction angle e0. The surrounding rock pressure e1 decreases with the increase in lateral pressure coefficient e2, while surrounding rock pressure e3 increases with the increase in lateral pressure coefficient e3.

Keywords: deep-buried chamber; failure mode; surrounding rock pressure; numerical simulation; upper bound solution

MSC: 30A05



Academic Editors: Fernando Simoes and Carlos Conceicao Antonio

Received: 11 November 2024 Revised: 24 December 2024 Accepted: 25 December 2024 Published: 28 December 2024

Citation: Zhang, D.; Zeng, L.; Lv, Z.; Yu, X.; Liu, C.; Jiang, A.; Jiang, X.; Li, Q.; Yang, Y. Failure Mode of Deep-Buried Rectangular Chamber and Upper Bound Solution of Surrounding Rock Pressure.

Mathematics 2025, 13, 69. https://doi.org/10.3390/math13010069

Copyright: © 2024 by the authors. Licensee MDPI, Basel, Switzerland. This article is an open access article distributed under the terms and conditions of the Creative Commons Attribution (CC BY) license (https://creativecommons.org/licenses/by/4.0/).

1. Introduction

The stability of deep-buried rectangular chambers has always been a hot issue in the geotechnical field. In recent years, the stability of deep chambers has been paid more and more attention by scholars and engineers with the rapid development of underground transportation and mineral exploitation. A series of achievements have been made in the study of the stability of deep-buried chambers [1–4]. At present, the main methods to study the stability of underground chamber are the limit equilibrium method, the numerical simulation method, the model test method, and the limit analysis method. Different criteria of instability will lead to different results, and the differences are large. In addition, the complexity of geotechnical materials, the selection of boundary conditions, the division of mesh shape, and the determination of initial conditions will affect the accuracy of calculation results. In the model test, because of the acceleration of the centrifuge, the start-up and braking will affect the experimental results. In the process of the simulation

Mathematics 2025, 13, 69 2 of 14

test, it is difficult to accurately simulate the real situation of the model, including model boundary, constraints, construction process, support form of support components, and support parameters. The stress of deep-buried chambers is complex, and the process of elastic–plastic analysis of a chamber step by step is rather tedious. Unlike the limit equilibrium method, the limit analysis theory does not need to consider the stress–strain state and complex load conditions in the process of chamber deformation, and it can solve the ultimate load of chamber failure from the point of view of energy. Thus, a more accurate solution can be obtained than from these methods.

At present, in the stability analysis of underground chambers, the solution of surrounding rock pressure based on limit analysis is widely accepted and used by academia [5–7]. Yang et al. [8] established a two-layer model of collapse block shape of a rectangular tunnel. The upper bound solution of the surrounding rock pressure was obtained and the continuous failure mechanism of the deep cavity roof collapse was deduced by using the upper bound solution. Huang et al. [9] used limit analysis theory to analyze the three-dimensional stability of a circular tunnel working face in a heterogeneous anisotropic undrained clay. The critical collapse support pressure and stability ratio of the tunnel were obtained. Zhao et al. [10] used the upper bound theorem to analyze the stability of irregular underground caverns. The influence of geological parameters of the irregular chamber on the mechanism of chamber collapse was given. Guan et al. [11] deduced the analytical expression of three-dimensional failure mode of an underground chamber by upper limit theorem.

The numerical solution of the collapse block shape of a circular tunnel was derived by Huang et al. [12] based on the Hoek-Brown failure criterion and the upper bound theorem. According to the upper bound theorem and variational method, Qin et al. [13] constructed the progressive failure mechanism of the roof of a deep-buried tunnel. The analytical solution of the roof collapse pattern and the collapse area was derived, and the calculation results were verified. Fraldi and Guarracino [14] proposed and discussed the comprehensive analytical solution of a tunnel collapse mechanism with an arbitrary excavation section in a rock mass under the Hoek-Brown criterion. Perazzelli and Anagostou [15] used the upper bound theorem of limit analysis to analyze the shape of the failure surface of a gas storage tunnel when arch failure occurs. The influences of geometric parameters and geotechnical parameters on arching pressure were studied. Huang et al. [16] used the Hoek-Brown failure criterion and the upper bound theorem of limit analysis to study the shape of a collapse block of a square tunnel under pore water pressure. The analytical solution of the collapse block shedding curve was derived. Liu et al. [17] studied the stability of a deep-buried tunnel working face using the upper bound analysis method. By considering the seepage force on the tunnel face and soil particles, the upper bound solution of supporting pressure required for the stability of a layered seepage soil surface was obtained. A three-dimensional rotation-translation mechanism that simultaneously considers the longitudinal inclination of the tunnel and partial failure of the tunnel face based on the upper bound limit analysis method was presented [18]. Zhang et al. [19] proposed an improved failure mechanism for deep-buried caverns, and studied the supporting pressure of deep-buried caverns. The calculated results of the improved failure mechanism are in good agreement with the existing methods, numerical solutions, and field monitoring results.

This study systematically establishes the failure mechanism of rectangular deep-buried chambers and derives an upper bound analytical solution for the surrounding rock pressure based on limit analysis theory. Through in-depth exploration, the influence of various parameters, including geometric characteristics, material properties, and stress conditions, on the surrounding rock pressure and the chamber's failure mode are thoroughly analyzed. The results not only enhance the theoretical understanding of the mechanical behavior of

Mathematics 2025, 13, 69 3 of 14

deep-buried structures but also provide a robust framework for optimizing their design and stability evaluation. These findings are expected to serve as a foundational reference for engineering applications, promoting safer and more efficient construction practices in underground spaces.

2. Upper Bound Theorem of Limit Analysis

The principle of limit analysis includes two parts: the upper bound theorem and the lower bound theorem. This theory is a relatively effective method for solving stability problems in geotechnical engineering. Since its inception in the 1920s, this theory has been developing slowly and has mostly focused on the study of one-dimensional structural problems. Until the 1950s, the upper and lower limit theorems of limit analysis theory were confirmed, and the associated flow rule was proposed by Drucker. The application of limit analysis developed rapidly and was promoted in solving plane and space problems. After decades of development, this theory has been rapidly developed and widely applied in the analysis of foundation bearing capacity, slope, retaining wall, and tunnel stability in geotechnical engineering. Compared with traditional stability calculation theories in geotechnical engineering, such as the limit equilibrium method, the slip line method, and the finite element method, the limit analysis method has its unique features, because no matter how complex the geometric shape and load situation of the structure are, the limit analysis method can always obtain a practical failure load value and provide a clear physical graph of the failure mechanism.

According to the principle of virtual power, the upper limit theorem of limit analysis needs to satisfy the velocity boundary condition and the compatibility condition between strain and velocity. In the velocity field of motion permission, the load obtained based on the condition of equal internal and external power is greater than or equal to the actual ultimate failure load. In the upper limit theorem of limit analysis, it is not necessary to study whether the object satisfies the stress equilibrium condition, but only to calculate the external force power and calculate the internal energy dissipation rate according to the flow law, and the resulting load is one upper limit solution under this condition.

For arbitrary maneuvering admissible velocity field, the upper bound solution of failure load can be obtained according to the internal energy loss rate not less than the external force power. The expression is as follows [20]:

$$\int_{V} \sigma_{ij} \dot{\varepsilon}_{ij} dV \ge \int_{s} T_{i} v_{i} ds + \int_{V} F_{i} v_{i} dV, \tag{1}$$

In the above formula, T_i is the surface force acting on the surface area s of the damaged body. F_i is the physical force acting on the volume V of the damaged body. σ_{ij} is the stress field associated with F_i and T_i . v_i is the velocity field allowed by maneuver. $\dot{\varepsilon}_{ij}$ is the strain rate field compatible with v_i .

3. Construction of Failure Mode

Based on the kinematical approach of limit analysis, an improved failure mechanism is proposed, and the supporting pressure is investigated for a deep-buried cavity. Reference [19] proposed a cavity failure mode of "a wedge block + a rotational arc block + n translational triangular blocks". However, the destructive mode is too complex and not conducive to specific applications. In this paper, the failure mode constructed in reference [19] is improved. The failure mode of "downward sliding wedge-shaped collapse body + rotating arc body with apex angle as the center + logarithmic helix body with apex angle as the center" is constructed, as shown in Figure 1. The wedge-shaped block $ABGG_1B_1$ of the roof slides vertically downward at velocity v_0 . The rotational block BGC

Mathematics 2025, 13, 69 4 of 14

and $B_1G_1C_1$ with G and G_1 points as the center of the circle, respectively, have rotational failure. The logarithmic spiral region GCD and $G_1C_1D_1$ have rotational failure with G and G_1 as vertices, respectively. The surrounding rock pressures produced by the top and side walls of the chamber are g and g, respectively, and g = g = g = g = g and g = g

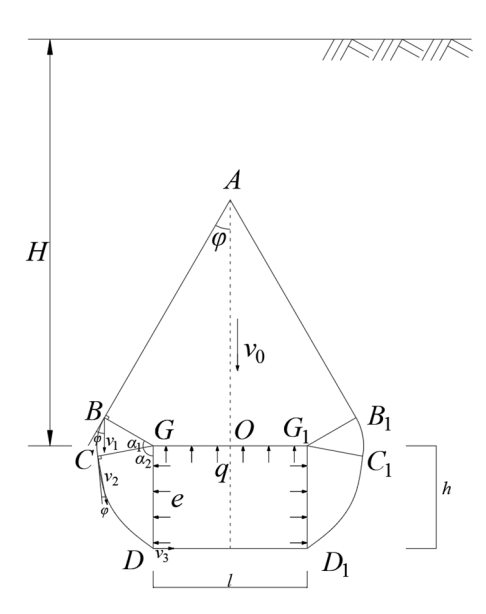


Figure 1. Schematic diagram of secondary stress distribution around the hole.

According to the geometric relationship and permissible velocity field for maneuvering, it can be seen that

$$GB = GC,$$
 (2)

According to the analysis of the velocity field in the arc radiation shear zone, it can be concluded that:

$$v_1 = v_0, (3)$$

$$v_2 = v_0 \exp[\alpha_1 \tan(2\varphi)],\tag{4}$$

According to the analysis of the velocity field of the logarithmic spiral radiation shear zone, it can be concluded that

$$v_3 = v_2 \exp(\alpha_2 \tan \varphi), \tag{5}$$

According to the recursive relationship of the length of the line breaks between different speeds, it can be concluded that

$$GC = \frac{GD}{\exp(\alpha_2 \tan \varphi)} = \frac{h}{\exp(\alpha_2 \tan \varphi)},$$
 (6)

$$AB = \frac{GB}{\tan \varphi} + \frac{l}{2\sin \varphi} = \frac{h}{\tan \varphi \exp(\alpha_2 \tan \varphi)} + \frac{l}{2\sin \varphi'}$$
 (7)

$$AO = AB\cos\varphi + GB\sin\varphi,\tag{8}$$

In the subsequent analysis, Equations (2)–(8) are very important foundations. Many formulas are derived from this equation.

4. Calculation Process

The analysis here operates under these assumptions: (1) No additional tunnels are near the research subject. (2) The surrounding rock mass is homogeneous. (3) The roadway's

Mathematics **2025**, 13, 69 5 of 14

cross-sectional shape is rectangle. Because the failure mode is symmetrical along *AO*, the solution of surrounding rock pressure can be obtained by calculating only the power of the left half of the failure mode:

4.1. Calculation of External Power

External power includes rock weight power and supporting reaction power.

The total gravity power of the rock body is the sum of three parts: quadrilateral *ABGO*, sector *GBC*, and logarithmic spiral *GCD*. The gravity power of each region can be obtained by multiplying the density, area, and velocity. The external power expression is as follows:

$$W = \gamma \cdot S \cdot v, \tag{9}$$

The formula for calculating the area of each rigid block is as follows:

$$S_{ABGO} = \frac{1}{2}BG \cdot AB + \frac{1}{2}AO \cdot GO, \tag{10}$$

$$S_{GBC} = \int_0^{\alpha_1} \frac{1}{2} GB^2 d\theta',\tag{11}$$

$$S_{GCD} = \int_0^{\alpha_2} \frac{1}{2} (GC \cdot \exp(\theta' \tan \varphi)) d\theta', \tag{12}$$

After calculating the area of each region, the gravity power can be calculated separately according to Equation (9).

The gravity power of the quadrilateral *ABGO* can be calculated by the following formula:

$$W_{ABGO} = \gamma \cdot S_{ABGO} \cdot v_1 = \gamma \cdot v_0 \cdot h^2 \cdot f_1, \tag{13}$$

For the sake of simplicity of the equation, f_1 is used to represent complex formulas. The expression of f_1 is as follows:

$$f_{1} = \left[\frac{h}{\tan \varphi \exp(\alpha_{2} \tan \varphi)} + \frac{l}{2 \sin \varphi}\right] \cdot \frac{1}{2h \exp(\alpha_{2} \tan \varphi)} + \frac{l}{4h} \cdot \left\{\left[\frac{1}{\tan \varphi \exp(\alpha_{2} \tan \varphi)} + \frac{l}{2h \sin \varphi}\right] \cdot \cos \varphi + \frac{\sin \varphi}{\exp(\alpha_{2} \tan \varphi)}\right\}$$
(14)

In sector region *GBC*, according to Figure 2, the expression of gravity power of rock mass can be obtained as follows:

$$W_{GBC} = \gamma \cdot S_{GBC} \cdot v_2 = \gamma v_0 h^2 f_2, \tag{15}$$

For the sake of simplicity of the equation, f_2 is used to represent complex formulas. The expression of f_2 is as follows:

$$f_2 = \frac{\exp[\alpha_1 \tan(2\varphi)][\tan(2\varphi)\cos\alpha_1 + \sin\alpha_1] - \tan2\varphi}{2\exp(2\alpha_2 \tan\varphi) \cdot (1 + \tan^22\varphi)},$$
(16)

In the logarithmic helix region *GCD*, according to Figure 3, the expression of gravity power of rock mass can be obtained as follows:

$$W_{GCD} = \gamma \cdot S_{GCD} \cdot v_3 = \gamma v_0 h^2 f_3, \tag{17}$$

Mathematics 2025, 13, 69 6 of 14

where the expression of f_3 is as follows:

$$f_{3} = \exp\left[\alpha_{1} \tan(2\varphi) - 2\alpha_{2} \tan\varphi\right] \cdot \frac{\exp(3\alpha_{2} \tan\varphi)\left[3 \tan\varphi \cos(\alpha_{1} + \alpha_{2} - \varphi) + \sin(\alpha_{1} + \alpha_{2} - \varphi)\right]}{2\left(1 + 9 \tan^{2}\varphi\right)} ,$$

$$-\frac{-3 \tan\varphi \cos(\alpha_{1} - \varphi) - \sin(\alpha_{1} - \varphi)}{2\left(1 + 9 \tan^{2}\varphi\right)}$$

$$(18)$$

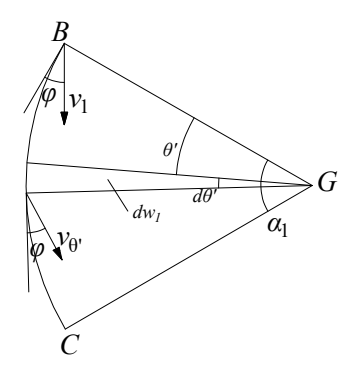


Figure 2. The power calculation schematic of circular arc zone *GBC*.

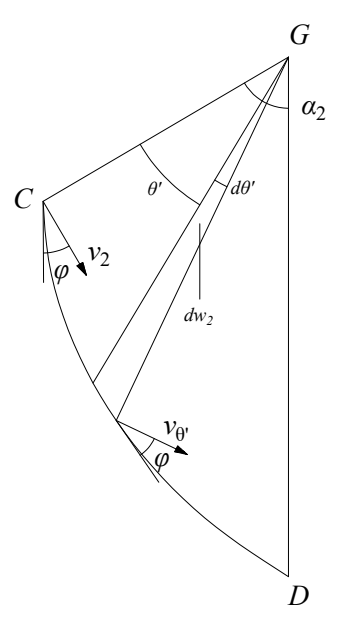


Figure 3. The power calculation schematic of logarithmic spiral zone *GCD*.

Support reaction power can be calculated by the following formula:

$$W_T = -q \cdot \frac{l}{2} \cdot v_0 - e \cdot h \cdot v_3 = -q \cdot \frac{l}{2} \cdot v_0 - Kq \cdot h \cdot v_2 \cdot \exp(\alpha_2 \tan \varphi) = -q v_0 h f_4, \quad (19)$$

The expression of f_4 is as follows:

$$f_4 = \frac{l}{2h} + K \cdot \exp[\alpha_1 \tan(2\varphi) + \alpha_2 \tan \varphi], \tag{20}$$

The total external power of the left half failure mode is the algebraic sum of the rock weight power and the support reaction power.

$$W_{ext} = W_{soil} + W_T = \gamma h^2 v_0 (f_1 + f_2 + f_3) - qhv_0 f_4, \tag{21}$$

Mathematics **2025**, 13, 69 7 of 14

4.2. Internal Energy Dissipation

Internal energy dissipation occurs on the velocity discontinuity line, the velocity discontinuity section, the circular arc shear zone, and the logarithmic spiral shear zone.

The expression of energy dissipation along the AB discontinuity line is as follows:

$$D_{AB} = c \cdot AB \cdot v_0 \cos \varphi$$

$$= c \cdot \left(\frac{h}{\tan \varphi \exp(\alpha_2 \tan \varphi)} + \frac{1}{2 \sin \varphi}\right) \cdot v_0 \cos \varphi ,$$

$$= cv_0 h f_5$$
(22)

where the expression of f_5 is as follows:

$$f_5 = \left(\frac{1}{\tan \varphi \exp(\alpha_2 \tan \varphi)} + \frac{l}{2h \sin \varphi}\right) \cdot \cos \varphi,\tag{23}$$

The energy dissipation of the arc shear plane BC and the arc shear zone GBC are

$$D_{BC} = \frac{c \cdot GB \cdot v_1 \cos \varphi}{\tan 2\varphi} \cdot \left\{ \exp[\alpha_1 \tan(2\varphi)] - 1 \right\}$$

$$= \frac{c \cdot h \cdot v_0 \cos \varphi}{\tan(2\varphi) \cdot \exp(\alpha_2 \tan \varphi)} \cdot \left\{ \exp[\alpha_1 \tan(2\varphi)] - 1 \right\} ,$$

$$= chv_0 f_6$$
(24)

$$D_{GBC} = \frac{c \cdot GB \cdot v_1 \cos \varphi}{\sin(2\varphi)} \cdot \{ \exp[\alpha_1 \tan(2\varphi)] - 1 \}$$

$$= \frac{c \cdot h \cdot v_0 \cos \varphi}{\sin(2\varphi) \cdot \exp(\alpha_2 \tan \varphi)} \cdot \{ \exp[\alpha_1 \tan(2\varphi)] - 1 \} ,$$

$$= chv_0 f_7$$
(25)

The expressions of f_6 and f_7 are

$$f_6 = \frac{\cos \varphi}{\tan(2\varphi) \cdot \exp(\alpha_2 \tan \varphi)} \cdot \{\exp[\alpha_1 \tan(2\varphi)] - 1\},\tag{26}$$

$$f_7 = \frac{\cos \varphi}{\sin(2\varphi) \cdot \exp(\alpha_2 \tan \varphi)} \cdot \{\exp[\alpha_1 \tan(2\varphi)] - 1\},\tag{27}$$

The expression of energy dissipation along the discontinuity line *CD* is the same as that in the whole logarithmic helical shear zone *GCD*.

$$D_{CD} = D_{GCD} = \frac{1}{2}c \cdot GC \cdot v_2 \cdot \cot \varphi \cdot \left[\exp(2\alpha_2 \tan \varphi) - 1\right]$$

$$= \frac{c \cdot h \cdot v_0 \exp[\alpha_1 \tan(2\varphi)] \cdot \cot \varphi}{2 \exp(\alpha_2 \tan \varphi)} \cdot \left[\exp(2\alpha_2 \tan \varphi) - 1\right] , \qquad (28)$$

$$= chv_0 f_8$$

The total internal energy dissipation in the left half of the failure mode is as follows:

$$D_{\text{int}} = D_{AB} + D_{BC} + D_{GBC} + D_{CD} + D_{GCD} = chv_1(f_5 + f_6 + f_7 + 2f_8), \tag{29}$$

4.3. Solution of Surrounding Rock Pressure

According to the virtual power principle, there are

$$W_{ext} = D_{int}, \tag{30}$$

The expression of surrounding rock pressure can be obtained as follows:

$$q = \frac{\gamma h(f_1 + f_2 + f_3) - c(f_5 + f_6 + f_7 + 2f_8)}{f_4},\tag{31}$$

Mathematics 2025, 13, 69 8 of 14

4.4. Confirmation of Constraints

In order to obtain the maximum pressure of the surrounding rock, it is necessary to optimize it under certain constraints. The physical parameters in the formula should conform to the characteristics of rock and rock materials, and the geometric parameters should have practical geometric significance. In summary, the following constraints can be determined:

s.t.
$$\begin{cases} 0 < \alpha_1 < \frac{\pi}{2} + \varphi \\ 0 < \alpha_2 < \frac{\pi}{2} + \varphi \\ \alpha_1 + \alpha_2 = \frac{\pi}{2} + \varphi \end{cases}$$
 (32)

Combined with the upper bound theorem, the sequential quadratic programming algorithm is used to solve the optimal solution of *q* by programming with Matlab 2020a.

5. Contrast Validation

The Protodyakonov falling arch theory is a formula for calculating the loosening pressure of loose strata and fractured rock mass, proposed by Russian scholar Протодъяконов in 1907. The Protodyakonov falling arch model is shown in Figure 4. The formula for calculating the surrounding rock pressure is as follows:

$$q = \gamma h_0, \tag{33}$$

$$h_0 = \frac{a_1}{f} = \frac{a + h \tan(45^\circ - \varphi/2)}{f},\tag{34}$$

In the formula, h_0 is the height of collapse arch, γ is the weight of rock mass, a is half of the width of tunnel, and f is the Protodyakonov coefficient.

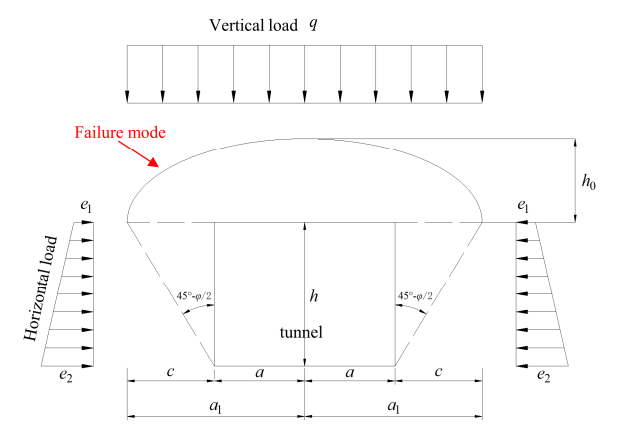


Figure 4. The schematic diagram of the Protodyakonov's theory.

Based on a large number of tunnel test results, Atkinson et al. [21] gave the failure mode of a tunnel as shown in Figure 5. In this failure mode, the wedge ABC slides downward at velocity v_0 . According to the limit analysis theory, the expression of the surrounding rock pressure q under the failure mode is as follows:

$$q = \frac{R\gamma[2 + \tan\varphi(2\varphi - \pi)] - 4c\cos\varphi}{4\sin\varphi},\tag{35}$$

In the formula, R is the radius of the circular tunnel, γ is the weight of the rock mass, c is cohesion, and φ is the internal friction angle.

Mathematics 2025, 13, 69 9 of 14

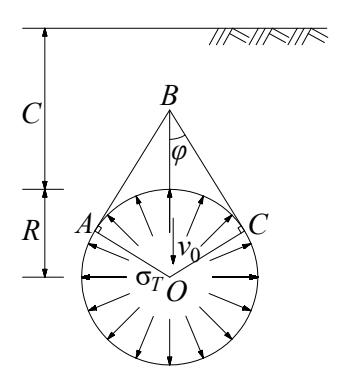


Figure 5. The failure mechanism of Atkinson et al. [21].

5.1. Numerical Simulation

In order to verify the scientificity of the failure mode of the deep chamber in this paper, the numerical simulation software FLAC3D 5.0 is used to verify the calculation. The calculated parameters are as follows: chamber height h=4 m, width l=6 m, c=10 kPa, $\varphi=30^\circ$, and lateral pressure coefficient K=1.0. The model has a width of 100 m in the horizontal direction and a thickness of 350 m in the vertical direction. The thickness in the axial direction of the vertical chamber is 10 m. The chamber is located at the center of the horizontal direction. The top is 300 m away from the upper boundary. The model is used to simulate the deformation of a 300 m deep chamber. Displacement constraints are applied to the front, back, left, right, and bottom of the model. The upper part is a free surface without constraints. Only the effect of gravity is considered in the calculation process. The parameters in the numerical simulation are shown in Table 1.

Table 1. Numerical model parameters.

Density (kg/m³)	Elastic Modulus GPa	Shear Modulus GPa	Tensile Strength MPa	Cohesion kPa	Friction Angle (°)	Poisson's Ratio	Bulk Modulus GPa
2560	2.37	1.21	1.89	10	30	0.3	5.33

Five sides of the model, the bottom and the front and back boundaries, are fixed. The meshes are divided into radial and rectangular hexahedral meshes around the cylinder. The shear strain increment maps obtained by numerical simulation are placed on the same map as the failure modes in this paper, which is shown in Figure 6.

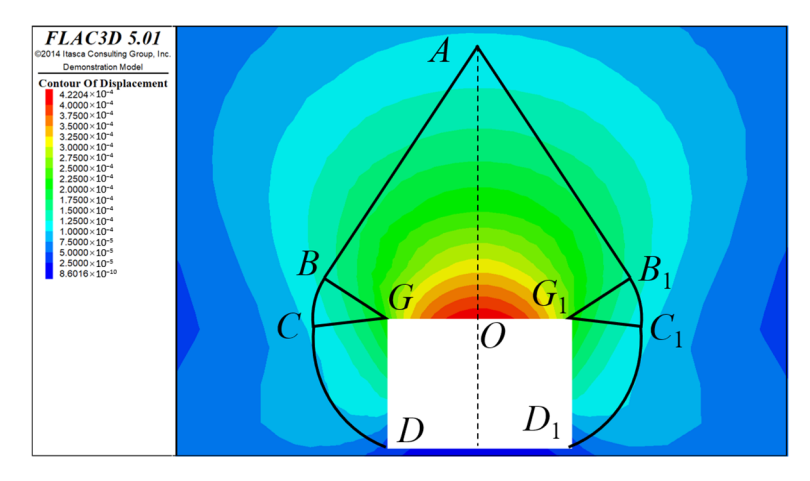


Figure 6. Comparisons between numerical simulation and failure mechanism in this paper.

Mathematics **2025**, 13, 69

From Figure 6, it can be concluded that the failure mode constructed in this paper is in good agreement with the failure area obtained by numerical simulation, which shows that the failure mode constructed in this paper is scientific and reasonable.

5.2. Comparative Verification

Combining the above three failure mechanisms, the following will theoretically verify the rationality of the calculation method in this paper. The parameters are as follows: $\gamma = 22 \text{ kN/m}^3$, chamber height h = 10 m, width l = 12 m, c = 25 kPa, and $\varphi = 20 \sim 25^\circ$. The surrounding rock pressure under each failure mechanism is calculated, which is compared with the calculated results and numerical simulation results in this paper. The comparison results are shown in Figure 7.

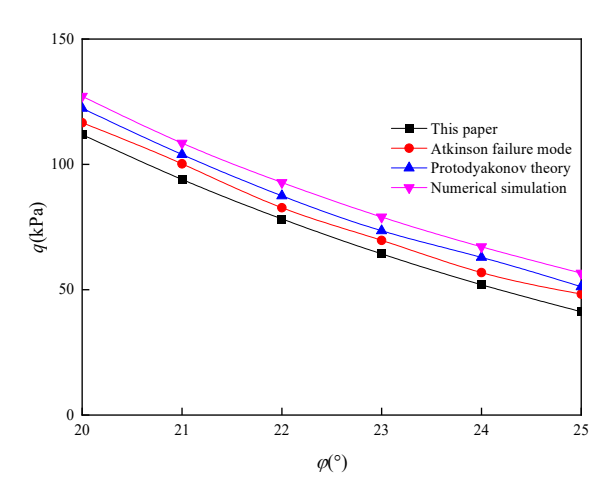


Figure 7. Comparison between this paper and other methods.

According to the six conditions under different internal friction angles (ϕ = 20~25°) in Figure 7, it can be concluded that the surrounding rock pressure calculated in this paper is less than that calculated by other methods. According to the upper bound theorem of limit analysis, it is shown that the surrounding rock pressure calculated in this paper is closer to the true solution of surrounding rock pressure and has higher accuracy than other theories. That is to say, the failure mode constructed in this paper is better.

5.3. Engineering Contrast

Taking Jiangyuanling Tunnel in Yueyang, Hunan Province, as the background, the rationality of this method is verified. Jiangyuanling Tunnel is a rock tunnel, and the rock is mainly strong weathered sericite sandy slate. According to the actual geological data, the relevant geological parameters are as follows: the rock mass weight $\gamma = 20 \text{ kN/m}^3$, c = 35 kPa, Poisson ratio $\mu = 0.4$, internal friction angle $\varphi = 21^\circ$, lateral pressure coefficient K = 1.0, tunnel width is 12 m, and height is 10 m. The result of the surrounding rock pressure calculated by this method is 54 kPa. In order to monitor the surrounding rock pressure during the tunnel construction, the pressure box is installed between the roof and the concrete support in the initial shotcrete support of the tunnel, and two pressure boxes are installed every 30 m to obtain the maximum monitoring results. The results of the surrounding rock pressure are shown in Table 2.

Table 2 shows that the error between the calculated results and the engineering monitoring results is less than 25%. The calculation results meet the engineering design requirements. At the same time, the rationality of the failure mode and the accuracy of the calculation results are verified.

Mathematics 2025, 13, 69 11 of 14

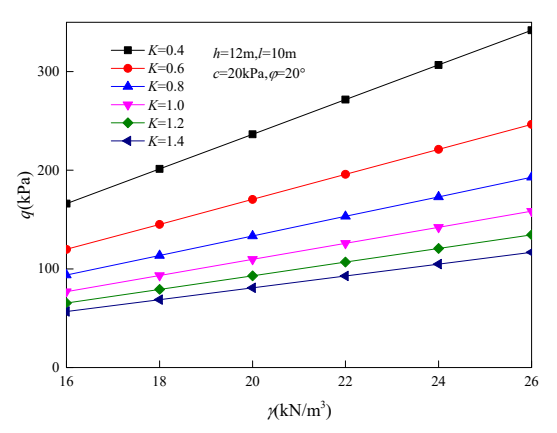
Number	Surrounding Rock Pressure (kPa)	The Results in This Paper (kPa)	Relative Error (%)
Monitoring point 1	47.6	54.4	12.5
Monitoring point 2	43.4	54.4	20.2
Monitoring point 3	44.5	54.4	18.2
Monitoring point 4	49.7	54.4	8.6
Monitoring point 5	46.6	54 4	14.3

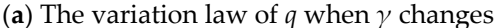
Table 2. Comparison between this paper and engineering.

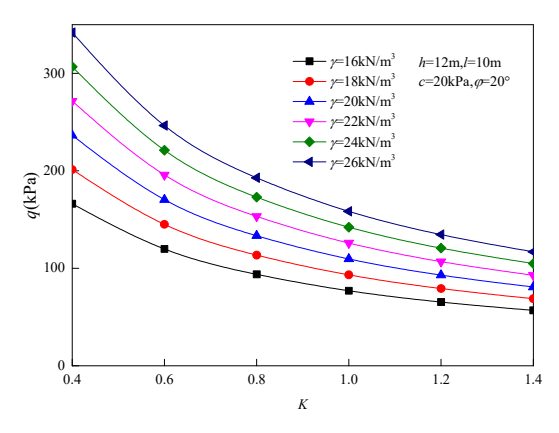
6. Result Analysis

Through the effects of rock gravity γ , the lateral pressure coefficient K, tunnel size, cohesion c, and internal friction angle φ on the surrounding rock pressure q and e are analyzed. The parameters are $\gamma = 16 \sim 26$ kN/m³, $K = 0.4 \sim 1.4$, tunnel height $h = 8 \sim 13$ m, width $l = 10 \sim 15$ m, $c = 18 \sim 28$ kPa, and $\varphi = 20 \sim 30^\circ$.

Through calculation, the influence of each parameter on the surrounding rock pressure is shown in Figures 8–11. From Figures 8 and 9, it can be concluded that the surrounding rock pressure q and e increase linearly with the increase in rock gravity γ . With the increase in lateral pressure coefficient K, the surrounding rock pressure q decreases nonlinearly and the surrounding rock pressure e increases nonlinearly. This shows that the buried depth of the tunnel has some influence on the surrounding rock pressure. From Figure 10, it can be seen that the surrounding rock pressure q and e increase linearly with the increase in the height and width of the tunnel, and the increasing trend is obvious. This shows that the tunnel size has a great influence on the surrounding rock pressure. From Figure 11, it can be seen that the surrounding rock pressure q and e decrease linearly with the increase in cohesion e. The surrounding rock pressure e and e decrease nonlinearly with the increase in internal friction angle e, and the reduction effect is obvious. This shows that the quality of the surrounding rock directly affects the magnitude of the surrounding rock pressure.



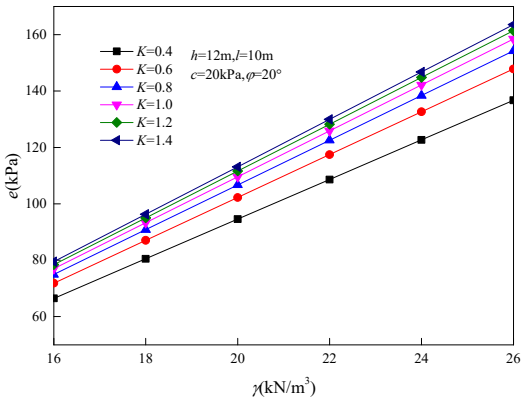


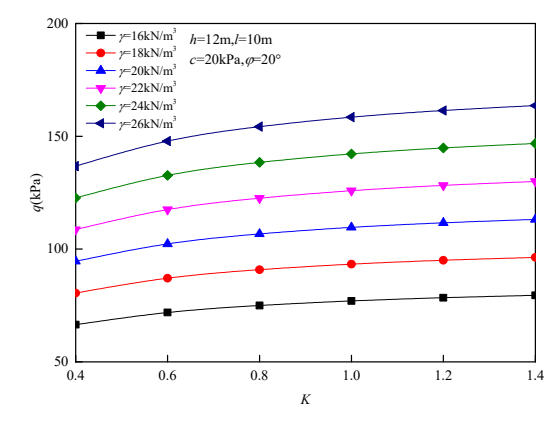


(b) The variation law of *q* when *K* changes

Figure 8. The influence of γ and K on surrounding rock pressure q.

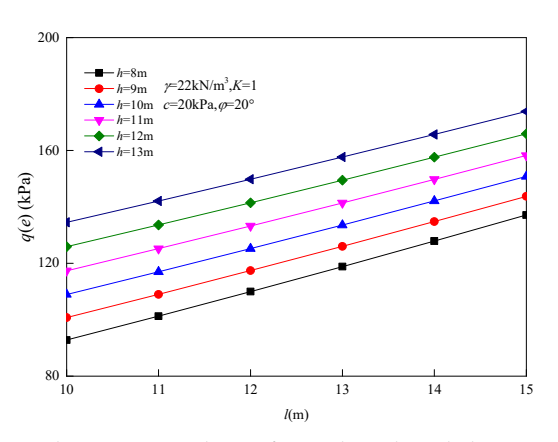
Mathematics 2025, 13, 69 12 of 14

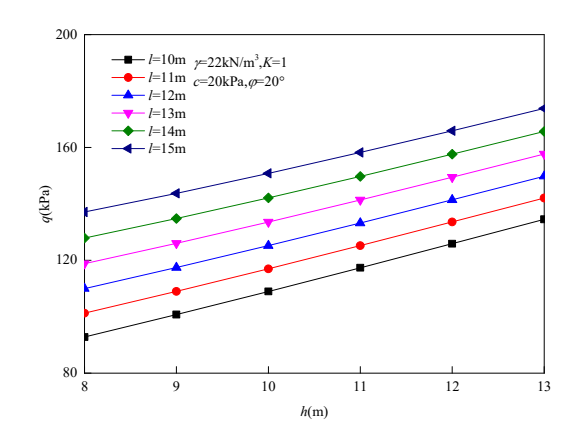




- (a) The variation law of e when γ changes
- **(b)** The variation law of *e* when *K* changes

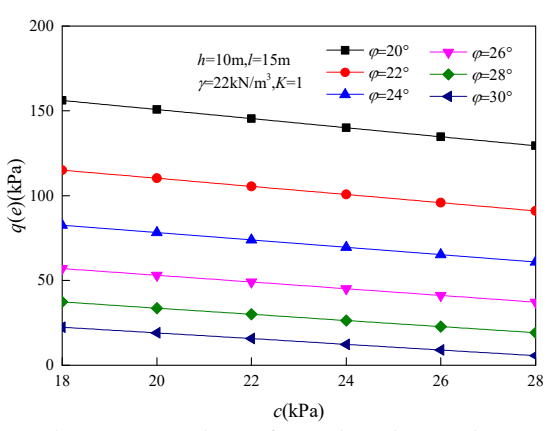
Figure 9. The influence of γ and K on surrounding rock pressure e and q.

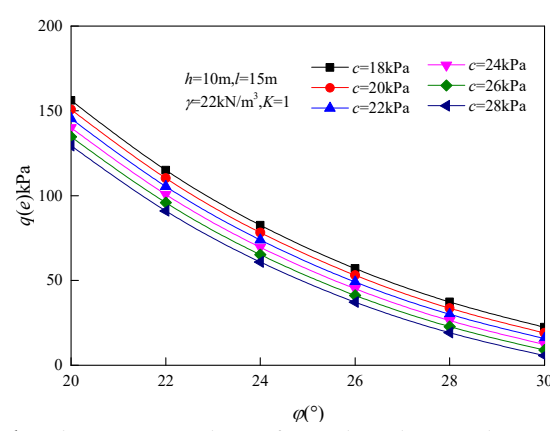




- (a) The variation law of q and e when l changes
- **(b)** The variation law of *q* and *e* when *h* changes

Figure 10. The influence of l and h on surrounding rock pressure q and e.





- (a) The variation law of *q* and *e* when *c* changes
- **(b)** The variation law of q and e when φ changes

Figure 11. The influence of *c* and φ on surrounding rock pressure *q* and *e*.

7. Conclusions

(1) It is reliable to calculate the surrounding rock pressure by using the failure mode of the deep-buried chamber in this paper. The surrounding rock pressure value calculated in this paper is a strict upper bound solution of the deep-buried chamber, which can be used as the theoretical basis for the excavation and support design and construction of the deep-buried chamber.

Mathematics 2025, 13, 69 13 of 14

(2) The surrounding rock pressure calculated by the failure model in this paper is less than that calculated by the Protodyakonov theory, Atkinson's failure model, and numerical simulation. It shows that the surrounding rock pressure calculated in this paper is closer to the real solution and has higher accuracy.

(3) Each parameter has a different influence on the surrounding rock pressure. The surrounding rock pressure q and e increase linearly with the increase in rock gravity γ and chamber size, and decrease with the increase in cohesion e and internal friction angle φ . The surrounding rock pressure e decreases with the increase in lateral pressure coefficient e0, while the surrounding rock pressure e0 increases with the increase in lateral pressure coefficient e1.

Author Contributions: Conceptualization, D.Z. and L.Z.; methodology, Z.L., X.Y. and C.L.; writing—original draft preparation, L.Z.; writing—review and editing, D.Z., A.J., X.J., Q.L. and Y.Y. All authors have read and agreed to the published version of the manuscript.

Funding: This research was funded by the National Natural Science Foundation of China, grant number 52074116 and 51804113 (Daobing Zhang). The financial support is greatly appreciated.

Data Availability Statement: The data presented in this study are available on request from the corresponding author. The data are not publicly available due to the complexity of the data.

Conflicts of Interest: Authors Zhilin Lv, Xiaochuan Yu and Chang Liu were employed by the company China Gezhouba Group Road & Bridge Co., Ltd. The remaining authors declare that the research was conducted in the absence of any commercial or financial relationships that could be construed as a potential conflict of interest.

References

- 1. Lenz, G.; Poisel, A.; Brandtner, M.; Goricki, A.; Wagner, O.K. Semmering Base Tunnel—Geotechnical models in design and construction. *Geomech. Tunn.* **2018**, *11*, 559–565. [CrossRef]
- 2. Tellioglu, V. Observations on cracking in concrete tunnel segments—An assessment of correlations. *Geomech. Tunn.* **2019**, 12, 82–95. [CrossRef]
- 3. Zhu, X.; Chen, Z.; Ren, Y. Numerical simulation study on the anchorage mechanism of yield supporting in deep tunnel. *Geotech. Geol. Eng.* **2018**, 37, 2091–2102. [CrossRef]
- 4. Bobet, A. Deep tunnel in transversely anisotropic rock with groundwater flow. *Rock Mech. Rock Eng.* **2016**, 49, 4817–4832. [CrossRef]
- 5. Cheng, H.Z.; Chen, J.; Chen, R.P.; Chen, G.L. Reliability study on shield tunnel face using a random limit analysis method in multilayered soils. *Tunn. Undergr. Space Technol.* **2019**, *84*, 353–363. [CrossRef]
- 6. Zuo, J.P.; Ma, Z.Y.; Xu, C.Y.; Zhan, S.F.; Liu, H.Y. Mechanism of principal stress rotation and deformation failure behavior induced by excavation in roadways. *J. Rock Mech. Geotech. Eng.* **2024**, *16*, 4605–4624. [CrossRef]
- 7. Kumar, A.; Chauhan, V.B. Advanced finite element limit analysis and machine learning for assessing the stability of square tunnels in rock slope. *Transp. Infrastruct. Geotechnol.* **2024**, *11*, 1928–1962. [CrossRef]
- 8. Yang, X.L.; Zhou, T.; Li, W.T. Reliability analysis of tunnel roof in layered Hoek-Brown rock masses. *Comput. Geotech.* **2018**, 104, 302–309. [CrossRef]
- 9. Huang, M.; Tang, Z.; Zhou, W.; Yuan, J. Upper bound solutions for face stability of circular tunnels in non-homogeneous and anisotropic clays. *Comput. Geotech.* **2018**, *98*, 189–196. [CrossRef]
- 10. Zhao, L.; Huang, S.; Zhang, R.; Zuo, S. Stability analysis of irregular cavities using upper bound finite element limit analysis method. *Comput. Geotech.* **2018**, *103*, 1–12. [CrossRef]
- 11. Guan, K.; Zhu, W.C.; Niu, L.L.; Wang, Q.Y. Three-dimensional upper bound limit analysis of supported cavity roof with arbitrary profile in Hoek-Brown rock mass. *Tunn. Undergr. Space Technol.* **2017**, *69*, 147–154. [CrossRef]
- 12. Huang, F.; Yang, X.L. Upper bound limit analysis of collapse shape for circular tunnel subjected to pore pressure based on the Hoek–Brown failure criterion. *Tunn. Undergr. Space Technol.* **2011**, 26, 614–618. [CrossRef]
- 13. Qin, C.B.; Yang, X.L.; Pan, Q.J.; Sun, Z.B.; Wang, L.L.; Miao, T. Upper bound analysis of progressive failure mechanism of tunnel roofs in partly weathered stratified Hoek–Brown rock masses. *Int. J. Rock Mech. Min. Sci.* **2015**, 74, 157–162. [CrossRef]
- 14. Fraldi, M.; Guarracino, F. Analytical solutions for collapse mechanisms in tunnels with arbitrary cross sections. *Int. J. Solids Struct.* **2010**, 47, 216–223. [CrossRef]

Mathematics 2025, 13, 69 14 of 14

15. Perazzelli, P.; Anagnostou, G. Upper bound limit analysis of uplift failure in pressurized sealed rock tunnels. *Int. J. Numer. Anal. Methods Geomech.* **2017**, 42, 719–735. [CrossRef]

- 16. Huang, F.; Zhang, D.B.; Sun, Z.B.; Wu, B. Influence of pore water pressure on upper bound analysis of collapse shape for square tunnel in Hoek-Brown media. *J. Cent. South Univ.* **2011**, *18*, 530–535. [CrossRef]
- 17. Liu, W.; Albers, B.; Zhao, Y.; Tang, X.-W. Upper bound analysis for estimation of the influence of seepage on tunnel face stability in layered soils. *J. Zhejiang Univ.-SCIENCE A* **2016**, *17*, 886–902. [CrossRef]
- 18. Ye, Y.L.; Lu, Z.W.; Sun, Y.Z.; Shang, S.J.; Qian, Z.J. Upper bound solution of passive instability on the face of longitudinal inclined shallow buried shield tunnel based on rotation–translation mechanism. *Comput. Geotech.* **2023**, *159*, 105473. [CrossRef]
- 19. Zhang, D.B.; Liu, Z.Z.; Zhang, J.H. A new failure mechanism for deep cavity and upper bound solution of supporting pressure. *J. Cent. South Univ.* **2017**, 24, 2082–2091. [CrossRef]
- 20. Zuo, J.; Ma, Z. Asymmetric deformation and failure behavior of roadway subjected to different principal stress based on biaxial tests. *Tunn. Undergr. Space Technol.* **2025**, 155, 106174. [CrossRef]
- 21. Atkinson, J.H.; Potts, D.M. Stability of a shallow circular tunnel in cohesionless soil. *Géotechnique* 1977, 27, 203–215. [CrossRef]

Disclaimer/Publisher's Note: The statements, opinions and data contained in all publications are solely those of the individual author(s) and contributor(s) and not of MDPI and/or the editor(s). MDPI and/or the editor(s) disclaim responsibility for any injury to people or property resulting from any ideas, methods, instructions or products referred to in the content.